CrossMark

A High Resolution Digital Image Correlation Study under Multiaxial Loading

E. Polatidis [1] · W.-N. Hsu [1,2] · M. Šmíd [1] · H. Van Swygenhoven [1,2]

Abstract
In this study, a miniaturized cruciform-shaped sample geometry which allows reaching high plastic strain under equibiaxial loading with reduced thickness at the test section is presented. The thinning method results in excellent surface quality that can be used for electron backscatter diffraction (EBSD) and high-resolution digital image correlation (HRDIC) investigations. The new cruciform geometry is used to study the slip activity in metastable austenitic stainless steel 304 during uniaxial and equibiaxial deformation using HRDIC. The results are discussed with respect to the Schmid law and the effect of multiple slip activity on the nucleation of martensitic transformations.

Keywords Digital image correlation · Multiaxial · Slip · TRIP · Schmid

Introduction

Metals and alloys are subjected to biaxial stresses and strain path changes during sheet forming, drawing processes and under service conditions. Under these complex loading conditions, the deformation behavior and the mechanical properties can differ from those obtained under uniaxial loading conditions [1, 2]. The origin of such strain path dependence has to be found at the inter- and intra-granular level and hence understanding the materials deformation behavior requires a thorough characterization at these length scales [3]. Dislocation slip is an inherent anisotropic mechanism and upon strain path changes anisotropic dislocation substructures develop. Moreover, other deformation mechanisms such as twinning and/or deformation-induced phase transformations occur e.g. in transformation induced plasticity (TRIP) steels [1, 4–9]. Since these mechanisms depend not only on materials parameters but also on the resolved shear stress, their activation depends on the strain path.

To gain insight into the dependence of the mechanical behavior on the strain paths, several biaxial deformation devices, using cruciform-shaped samples, have been employed in combination with microscopy, X-ray and neutron diffraction methods [4, 10–17]. Significant work has been done to optimize the cruciform geometries in order to reach high plasticity at the center, avoid fracture at the cruciform arms, reduce the stress heterogeneity in the center of the cruciform and prevent shear loading in the cruciform arms [18]. It is commonly known that in order to reach high enough plasticity (i.e. >5% equivalent von Mises strain) at the place of observation, the center of a cruciform sample has to be thinned. This can be achieved by machining or laser ablation. The surface quality which can be obtained by these methods is good enough for e.g. X-ray diffraction techniques but not sufficiently good for being used in microscopy studies such as electron backscatter diffraction (EBSD).

Recently a miniaturized biaxial tensile device that can be installed on synchrotron beamlines and inside scanning electron microscopes (SEMs) has been developed [17]. The implementation in an SEM allows performing in-situ deformation studies while undertaking high-resolution digital image correlation (HRDIC). The latter provides full-field displacement maps at high magnification upon deformation and has been successfully employed for studying deformation mechanisms, strain partitioning and crack propagation under uniaxial loading tests using dogbone-shaped samples [19–27]. A flat cruciform geometry has been used in combination with HRDIC to investigate the martensitic transformation of

✉ H. Van Swygenhoven
helena.vanswygenhoven@psi.ch

[1] Photons for Engineering and Manufacturing Group, Swiss Light Source, Paul Scherrer Institute, CH-5232 Villigen PSI, Switzerland

[2] Neutrons and X-rays for Mechanics of Materials, IMX, École Polytechnique Fédérale de Lausanne, CH-1015 Lausanne, Switzerland

superelastic NiTi in [11], where it was seen that the flat geometry can be used for performing uniaxial and strain path changes, but it does not allow reaching high plastic strains at the center of the sample under equibiaxial loading.

Here we present an optimized cruciform shape geometry which enables performing in-situ SEM biaxial tests coupled with HRDIC analysis. The sample is fabricated using electrochemical micromachining (ECMM), a micromachining method providing high surface quality which can be readily used for metallography characterization [28], and a picosecond laser for cutting the outline of the sample. The novel sample preparation method employed on a foil of austenitic stainless steel 304 (SS304) gives the possibility to reach high plastic deformation strains under uniaxial and equibiaxial load paths. The localization of plastic strain at the microstructural scale under uniaxial and biaxial strain conditions are discussed with respect to the obedience to the Schmid law for the activation of the slip systems within individual grains.

Experimental Procedure

Cruciform Samples

The optimization of the cruciform sample geometry is carried out with finite element simulations using the commercial ABAQUS/Standard software [29]. The stress-strain curve and isotropic elastic properties of SS304 obtained from uniaxial loading of a dogbone sample are used as materials properties input to the built-in model based on the Von Mises yield criterion and the associated flow rule [18]. Figure 1a shows the optimized geometry and a close view of the central pocket exhibiting a gradual thinning from 150 μm (arm) down to 40 μm (center). In order to improve the computational efficiency, only 1/8th of the entire cruciform geometry is simulated with symmetric boundary conditions being applied on the appropriate surfaces. A structured hexahedron mesh is employed with linear 8-node C3D8 elements as shown in Fig. 1b. The simulations are done with a linear loading

(surface traction mode) to a target force of 35 N on each arm along 500-time steps. The forces are applied on the inside area of the holes at the arms; the arrows in Fig. 1b indicate the loading directions.

A SS304 foil of 150 μm thickness in annealed state with a mean grain size of 19 ± 5 μm, excluding the annealing twins, was purchased from Goodfellow, UK. The rounded-square pockets are fabricated with ECMM carried out at micropat SA, Switzerland on both surfaces of the foil [30]. First, an epoxy-based resist (KMPR 1010) is applied onto the foil by spin coating at 3000 rpm, followed by soft baking at 100 °C for 20 min and hard baking at 180 °C for 20 min. After curing, this layer (~10 μm) is locally exposed to a short-pulse UV laser (Spectra Physics Explorer 355 nm) to define the rounded-square openings to the underlying metal surface. The unprotected areas are neatly etched at the rate of 2.08×10^{-2} mm^3/C in the 3 M sulphuric acid-methanol solution at room temperature. A "bathtub-like" depth profile in the pocket (Fig. 1a) and a smooth surface are obtained with high dimensional accuracy and good top-bottom pocket alignment. More details on the technique and its limitations can be found in [31–]. After completion of the electrochemical dissolution, the protective coating is stripped in N-Methyl-2-pyrrolidone (NMP) at 100 °C. Once the pockets are introduced to the foil, the outline of the cruciform is cut using a frequency tripled Nd:YAG picosecond pulsed laser at the Swiss Federal Laboratories for Materials Science and Technology (EMPA). The power of the laser for cutting is 870 mW with 160 kHz pulse frequency, a pulse width of 10 ps and wavelength of 355 nm is used.

The above described sample preparation method ensures the material to retain the austenitic phase, i.e. avoiding the martensitic transformation induced by the deformation during mechanical surface preparation. Furthermore, no recrystallization, carbide formation or surface oxidation is to be expected at the temperatures used (i.e. maximum temperature of 180 °C). Figure 2 shows the high surface quality achieved by the ECMM process, the polycrystalline microstructure can be clearly revealed by secondary electron (SE) imaging with SEM.
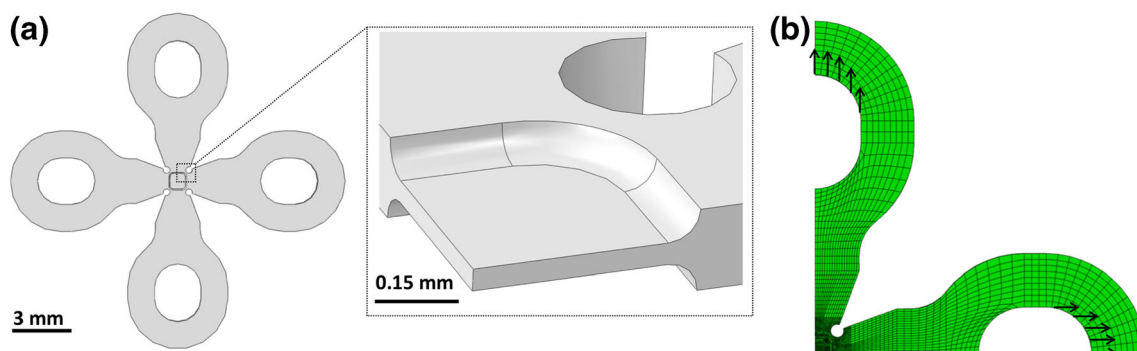

Fig. 1 (a) Schematics of the cruciform shaped sample with a detailed view of the pocket. (b) The finite element mesh with C3D8 element used for 1/8th of the cruciform geometry. The arrows indicate the direction of the applied load

Fig. 2 (a) Optical microscopy image and (b) secondary electron (SE) image from SEM showing the smooth and high surface quality after the sample preparation by ECMM. (c) High magnification SE imaging of the polycrystalline microstructure
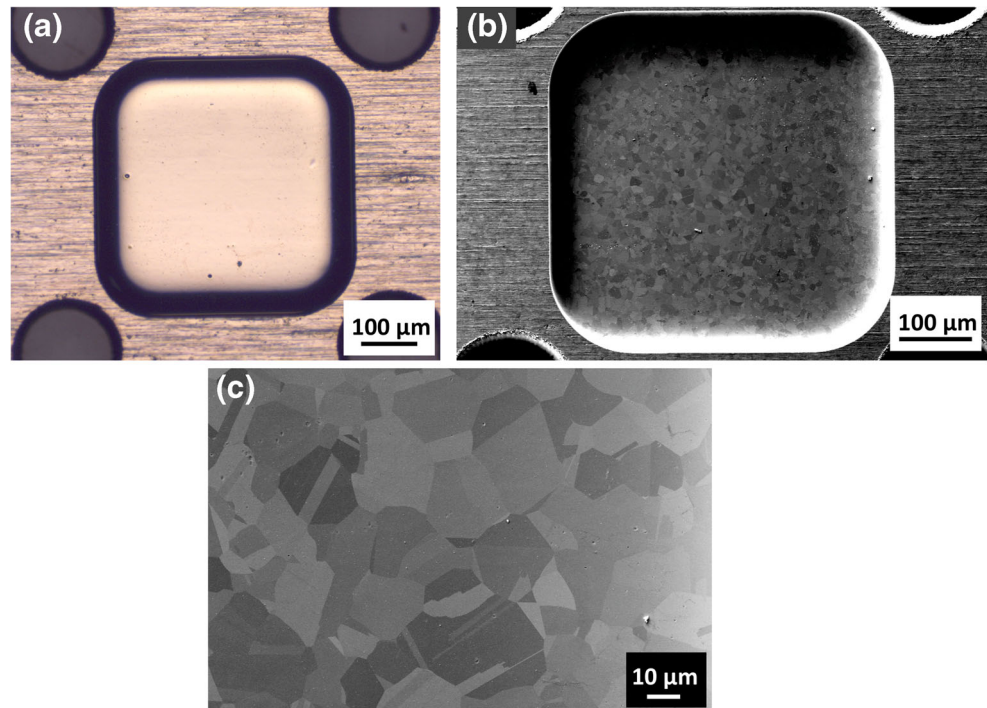
Macroscopic Digital Image Correlation

In order to study the force-strain response of the cruciform samples under uniaxial and equibiaxial load paths, deformation tests using a mini-biaxial machine developed at Paul Scherrer Institute [17] are performed in combination with macroscopic digital image correlation (macro-DIC) analysis. The ECMM thinning process produces a mirror-like surface that does not give reflections to serve as DIC pattern. Therefore, the surface obtained from ECMM is slightly etched with solution of 170 ml H_2O, 230 ml HCl and 20 ml HNO_3 for 5 min in order to introduce surface roughness, which serves as the surface features to be tracked for the macro-DIC analysis. During the displacement-controlled deformation (displacement rate 0.4 µm/s), series of images (with a resolution of 2484×3840 pixels) are taken at the center of the cruciform (field of view, FOV, of 0.9×1.38 mm^2) using a PixeLINK camera. The analysis of the DIC data is undertaken using the open source 2D-DIC software Ncorr [33]. The average equivalent strain is calculated from an area of 150 µm × 150 µm at the center of the pocket (see Fig. 3) using the relationship:

$$\varepsilon_{eq} = \frac{2}{3} \times \frac{1}{\sqrt{2}} \sqrt{\left(\varepsilon_x - \varepsilon_y\right)^2 + \left(\varepsilon_y - \varepsilon_z\right)^2 + \left(\varepsilon_z - \varepsilon_x\right)^2 + 6\varepsilon_{yz}^2 + 6\varepsilon_{zx}^2 + 6\varepsilon_{xy}^2}$$

(1)

where ε_x, ε_y are the two in-plane strain components and ε_{xy} is the shear strain obtained by DIC analysis. ε_{yz} and ε_{zx} are taken as zero and ε_z is taken as:

$$\varepsilon_z = -\left(\varepsilon_x + \varepsilon_y\right)$$

(2)

EBSD

The high surface quality of the pocket after ECMM makes it suitable for EBSD mapping without further preparation. EBSD studies of the initial microstructure (undeformed) are undertaken at the center of the cruciform pocket. The area of interest for the HRDIC study is mapped for two samples, one that will be deformed under uniaxial and the other under equibiaxial load paths. The EBSD maps are acquired with a field emission gun (FEG) SEM Zeiss ULTRA 55 equipped
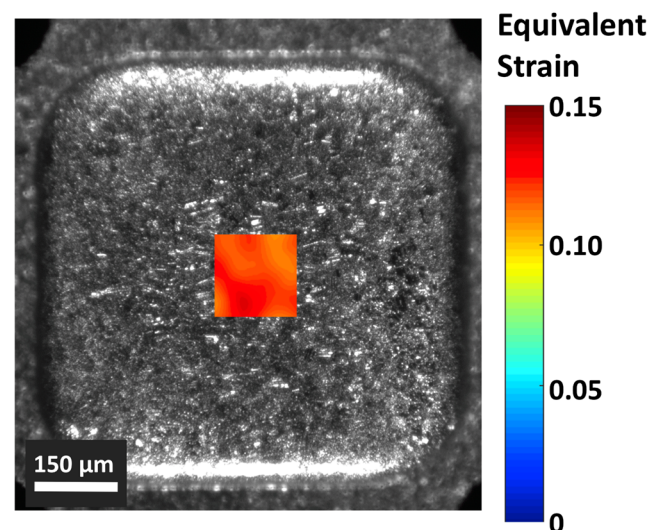

Fig. 3 The equivalent strain calculated with Eq. 1 from the strain components obtained from macro-DIC at the center of the cruciform, a global strain is averaged over an area of 150 µm × 150 µm (global strain ~14%)
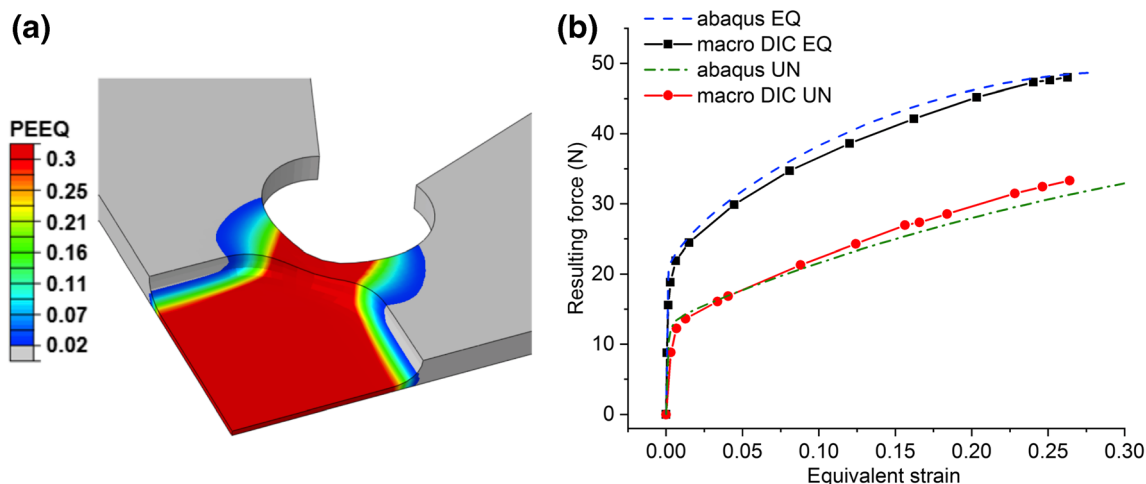
Fig. 4 (a) FE simulation of equibiaxial load results in high equivalent plastic strain (PEEQ) at the center of the pocket. (b) Comparison between experimental results from macro-DIC and FE analysis for uniaxial and equibiaxial loading

with an EDAX Hikari Camera, at 20 kV in high current mode with a 120 μm aperture. The EDAX OIM Analysis 7.3 software is used for post-processing the EBSD raw data and plotting the {111} traces in each grain and to reveal the average Schmid factor of all slip systems under uniaxial or equibiaxial loading.

HRDIC

The fine gold speckle pattern for HRDIC is obtained by the remodeling process of a thin gold layer [20] deposited on the mirror-like surface obtained from ECMM. For the in-situ HRDIC measurements, the mini-biaxial machine is installed inside the chamber of a FEG SEM Zeiss ULTRA 55. The deformation tests are performed in displacement control with a displacement rate of 0.4 μm/s. The electron beam with acceleration voltage of 3 kV in combination with a 20 μm aperture is used for the image acquisition. The images are acquired

with an in-lens detector at a working distance (WD) of 7.5 mm in order to minimize the topographic contrast by gathering low energy electrons, providing a good signal/noise ratio.

The force-strain response obtained from macro-DIC is used to decide the force values at which HRDIC is performed. Hence both in-situ uniaxial and equibiaxial tests with SEM can be monitored at the same equivalent strains. SEM images are taken at 2500× magnification with a resolution of 3072 × 2304 pixels (the FOV is 41 × 30.8 μm^2) at the center of the cruciform after reaching global equivalent strains of 2%, 6%, 10% and 14%. The total FOV consists of 4, slightly overlapping, images (2 × 2 grid) that cover an area of 78 × 55 μm^2. The HRDIC data is analyzed with Ncorr [33], using a subset radius of 15 pixels, 0 subset spacing and a strain radius of 3 pixels. These settings give a virtual strain gauge (VSG) of 1 pixel according to Ref. [34].

Thermal drifts and lens distortions in SEM imaging have been found to cause pseudo-strains in SEM DIC studies,

Fig. 5 Inverse pole figure color maps parallel to the loading direction of the area of interest showing grains 1–21 for the samples under (a) uniaxial load (IPF direction-2) and (b) equibiaxial load (IPF direction-3)
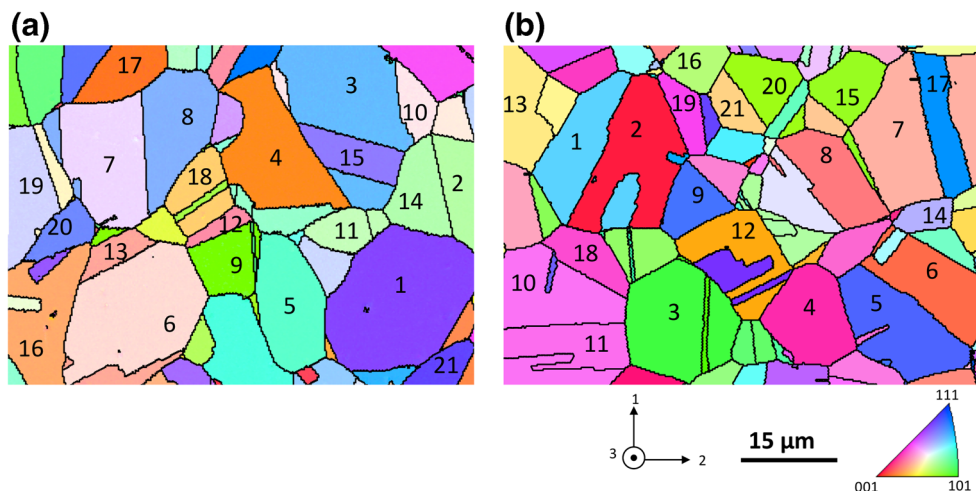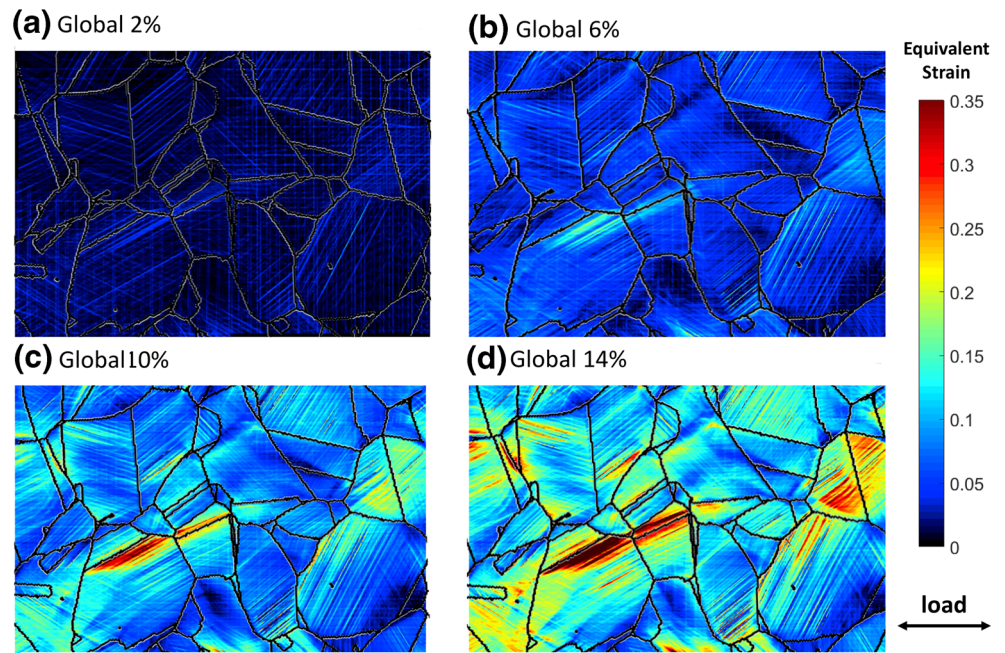
Fig. 6 HRDIC maps showing the evolution of slip activity upon uniaxial deformation at global equivalent strains of: (a) 2%, (b) 6%, (c) 10% and (d) 14%

methods for removing these artifacts and for obtaining reliable strain magnitudes have been suggested [35–40]. In order to investigate the drift distortions under the conditions of the HRDIC measurements, tests using a G-1 Si calibration grid from Pelcotec™ are performed before the cruciform tests. Two SEM images with a 10 min time gap between them are captured and analyzed with Ncorr following the guide and parameters in Ref. [35]. The analysis shows an average equivalent pseudo-strain of 0.11% due to thermal drifts within a 10 min time gap. This magnitude of pseudo-strain is low compared to the strain concentrations that are observed due to slip (typically in the range of ~10–35%), and do not affect the qualitative characterization of the activated slip systems which is based on the inclination of the slip traces. Hence, correcting the strain magnitude for the present analysis is not crucial.

Fig. 7 HRDIC maps showing the evolution of slip activity upon equibiaxial deformation at global equivalent strains of: (a) 2%, (b) 6%, (c) 10% and (d) 14%
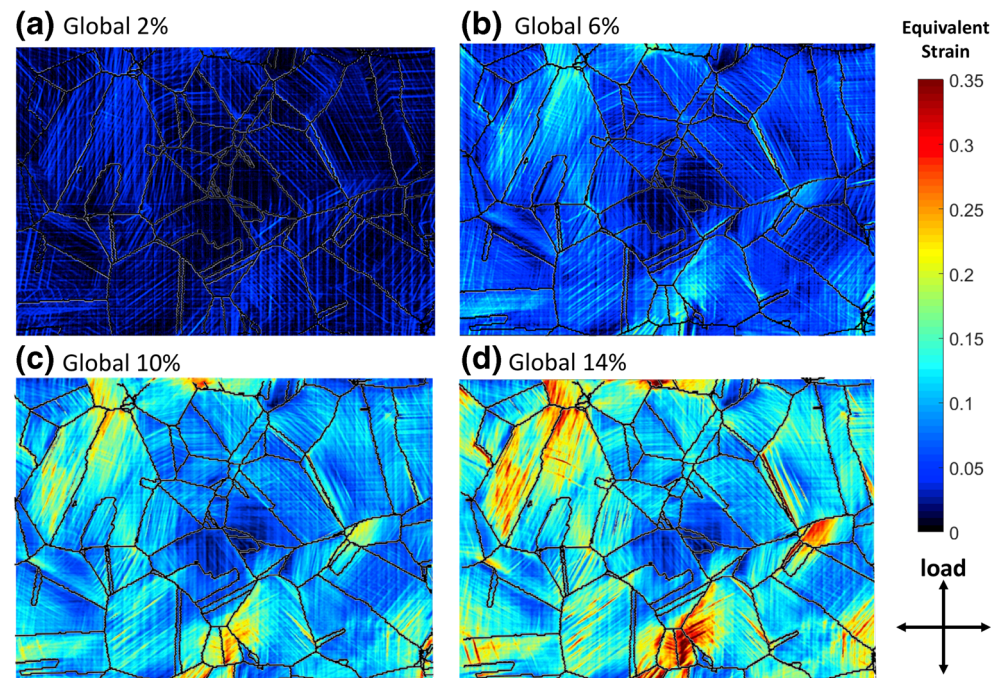
Results and Discussion

Force-Strain Response of Cruciform Samples

The simulation shown in Fig. 4a demonstrates that the cruciform geometry allows reaching more than 25% plastic strain in the center under equibiaxial loading. Figure 4b compares the force-strain curves obtained from simulations (dashed lines) and from macro-DIC analysis (solid lines) for both load paths confirming the capability of reaching high strain levels. The resulting force in the case of equibiaxial load is taken as $\sqrt{F_{axis\,1}^2 + F_{axis\,2}^2}$ from the corresponding force readings on the two axes. The FE simulation is able to capture the experimental data relatively well. Small deviations may occur due to: i) the development of texture during plastic deformation, whereas the simulation considers isotropic mechanical properties ii) small differences in sample geometry between the model and the experiment, due to tolerances in ECCM and laser-cutting and iii) the DIC providing only the strain components ε_{xx}, ε_{yy} and ε_{xy} to calculate the equivalent strain. The good match between simulation and experiment allows using the FE simulation for estimating the stress values at the center of the cruciform shaped specimens under the different loading conditions. This is known to be non-trivial as cruciform samples do not possess a well-defined cross-section as compared to uniaxial dogbone samples [10].

Slip Traces Observed with HRDIC

Figure 5 shows the EBSD map of the initially random texture of the fully austenitic microstructure. Figure 5a shows the area for which HRDIC images are taken under uniaxial deformation and Fig. 5b the area examined under biaxial deformation. The inverse pole figure (IPF) maps are shown with respect to the loading direction, i.e. along direction-2 under uniaxial loading (see the inset with the axes labels in Fig. 5) and along direction 3 for equibiaxial (equibiaxial loading along directions-1 and -2 is equivalent with compression along direction-3). In both areas the grains are labeled to facilitate further discussion related to the deformation mechanism. Figures 6 and 7 show the HRDIC maps obtained at 2%, 6%, 10% and 14% global strains under uniaxial and equibiaxial loads respectively. The above equivalent strain values correspond to respectively 355, 456, 543 and 624 MPa equivalent stress at the center of the cruciform, as calculated from the FE simulation of the corresponding load paths. Table 1 summarizes a relatively good agreement between the microscopic strain obtained from averaging the equivalent strain within the FOV of the HRDIC map and the macroscopic strain obtained from the macro-DIC.

The evolution of the plastic deformation within the FOV of HRDIC is evidenced by the increasing density and strain magnitude of the slip traces. Each grain exhibits its own slip traces with a characteristic trace inclination which corresponds to one of the possible {111} slip-plane traces. Tables 2 and 3 list the observed slip traces, the corresponding Schmid factor and the equivalent macro strain at which each slip trace is observed for the first time for the grains marked in Fig. 5a and b (uniaxial and equibiaxial loading respectively). Figure 8 shows an example of grain 1 under uniaxial loading for which

Table 1 Comparison of the global equivalent strain (from macroscopic DIC) and the equivalent strain averaged over the HRDIC field of view

Equivalent strain (%)

Global (macro-DIC)	Uniaxial HRDIC	Equibiaxial HRDIC
2	1.6	2
6	4.8	5.8
10	9.5	9.8
14	13.8	13.1

Table 2 List of activated {111}<110> systems and their Schmid Factor (SF) for each grain under uniaxial loading

Grain	Activated	Rank of SF	Equivalent strain seen (%)
1	(1–11)[0–1–1]	1 (0.3858)	2
	(111)[−110]	2 (0.3630)	10
2	(−11 1)[01–1]	1 (0.4842)	2
3	(1–1 1)[−1–10]	1 (0.4263)	2
4	(111)[01–1]	1(0.471)	2
5	(−111)[01–1]	1(0.4472)	2
6	(1–11)[−1–10]	1(0.4942)	2
	(11–1) [1–10]	2(0.4331)	2
7	(−111)[01–1]	1(0.4821)	2
	(1–11)[0–1–1]	2(0.3934)	2
8	(111)[01–1]	1(0.4376)	2
9	(1–11)[0–1–1]	1(0.4501)	2
10	(1–11)[0–11]	1(0.4908)	2
11	(1–11)[0–1–1]	1(0.4879)	2
12	(1–11)[−1–10]	2(0.4493)	2
13	(1–11)[0–1–1]	1(0.4944)	2
	(−111)[01–1]	2(0.4597)	10
14	(−111)[01–1]	1(0.4842)	2
15	(−111)[110]	1(0.4207)	2
	(−1–11)[0–1–1]	2(0.3369)	10
16	(−1–11)[0–1–1]	1(0.4927)	2
	(111)[01–1]	2(0.4760)	2
17	(1–11)[−1–10]	1(0.4615)	2
	(111)[01–1]	2(0.3935)	6
	(−111)[01–1]	3(0.3837)	10
18	(−1–11) [1–10]	1(0.4979)	2
	(1–11)[−1–10]	2(0.4799)	2
19	(−111)[01–1]	1(0.4748)	2
20	(1–11) [10-1]	1(0.4088)	2
21	(111)[0–11]	2(0.3319)	2

Table 3 List of activated {111}<110 > systems and their Schmid Factor (SF) for each grain under equibiaxial loading

| Grain	Activated system	Rank of SF (value)	Equivalent strain seen (%)
1	(−1−11)[011]	1(0.4296)	2
	(111)[−101]	3(0.2208)	6
2	(−1−11)[101]	1(0.4300)	2
	(1−11)[−101]	2(0.4284)	2
3	(−1−11)[101]	1(0.4196)	2
4	(111)[−101]	1(0.4596)	2
	(−111)[101]	3(0.4235)	2
5	(−111)[101]	1(0.3650)	2
	(1−11)[011]	2(0.3003)	2
6	(−1−11)[101]	1(0.4653)	2
	(1−11)[−101]	2(0.4599)	2
7	(1−11)[−101]	2(0.4575)	2
8	(−111)[101]	1(0.4811)	2
	(111)[−101]	2(0.4608)	2
9	(111)[0−11]	1(0.3696)	2
10	(−111)[0−11]	1(0.4651)	2
	(−1−11)[011]	3(0.3838)	2
11	(−1−11)[011]	1(0.4659)	2
	(111)[−101]	2(0.4150)	2
12	(−111)[101]	1(0.4814)	2
13	(−111)[0−11]	2(0.4749)	2
14	(111)[−101]	1(0.4580)	2
15	(111)[−101]	1(0.4708)	2
	(−111)[101]	2(0.4649)	6
16	(−111)[101]	1(0.4873)	2
	(111)[−101]	2(0.4541)	2
17	(−1−11)[101]	1(0.3751)	2
18	(−111)[101]	1(0.4631)	2
	(111)[−101]	3(0.4039)	10
19	(111)[0−11]	1(0.4522)	2
20	(−111)[0−11]	1(0.4733)	2
	(−1−11)[011]	2(0.4695)	10
21	(111)[−101]	1(0.4991)	2

the slip system (1−11)[0−1-1] with the highest SF (0.3858) is first observed at 2% global strain and the secondary slip

system (111)[−110] becomes pronounced only after 10% global strain. In some grains slip traces of two systems are already present at 2% strain (see Table 3).

The Schmid law is mostly respected during uniaxial and equibiaxial loading as previously reported for uniaxial deformation on SS301 and SS304 [19, 21]. Figure 9 shows a statistical analysis of the obedience to the Schmid law. More than 80% of the grains in the field of view exhibit primary activated slip systems with the highest SFs for both load paths (see Fig. 9a). Secondary or tertiary slip systems are observed in some grains; however, under equibiaxial loading multiple slip is observed in more grains than under uniaxial loading (see Fig. 9b). Under uniaxial loading, the second and third slip systems follow the Schmid ranking (see Fig. 9c), e.g. in grain 6 under uniaxial loading, two slip systems are observed: (1−11)[−1−10] with the highest SF (0.4942) and (11−1)[1−10] with the second highest SF (0.4331). Under equibiaxial load there are however a few grains for which this ranking is not followed as for instance in grains 1, 4, 10 and 18 (see Table 3 for details on the ranking). It should be noted that in the present analysis, grain interactions which can locally alter the stress state and activate other slip systems are neglected. Therefore, the behavior of the grains is described in terms of the Schmid law with respect to the macroscopic stress state.

Equibiaxial load is found to enhance the activation of multiple slip systems at the same equivalent strain as uniaxial load. Nearly 57% of the grains contain secondary or tertiary slip systems when subjected to equibiaxial load, whereas, under uniaxial loading, only 38% of the grains exhibit multiple slip systems (see Fig. 9b). This result is in good agreement with a previous study of SS304 austenitic stainless steel, where 10 out of 26 studied grains (38%) exhibit multiple slip systems under uniaxial tension [21]. The SS304 studied here is known to partially transform into martensite at equivalent strains larger than 20% [41]. It has been observed that the transformation occurs earlier under equibiaxial deformation than under uniaxial [41]. The activation of more slip systems suggests the existence of more shear band intercepts during equibiaxial deformation, hence providing more nucleation sites for martensite [42–44]. The present study supports well

Fig. 8 Grain 1 under uniaxial loading where the deformation changes from single slip to multiple activated slip systems with increasing strain. Superimposed are the {111} traces for the first highest (with red lines) and the second highest (with yellow lines) Schmid factor
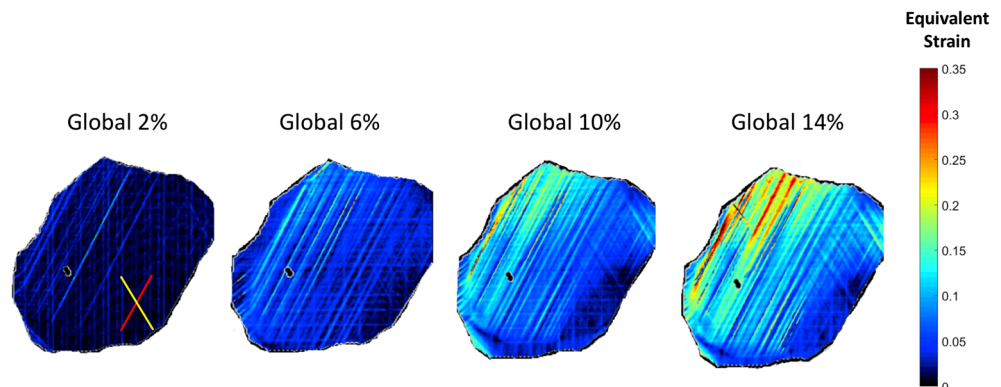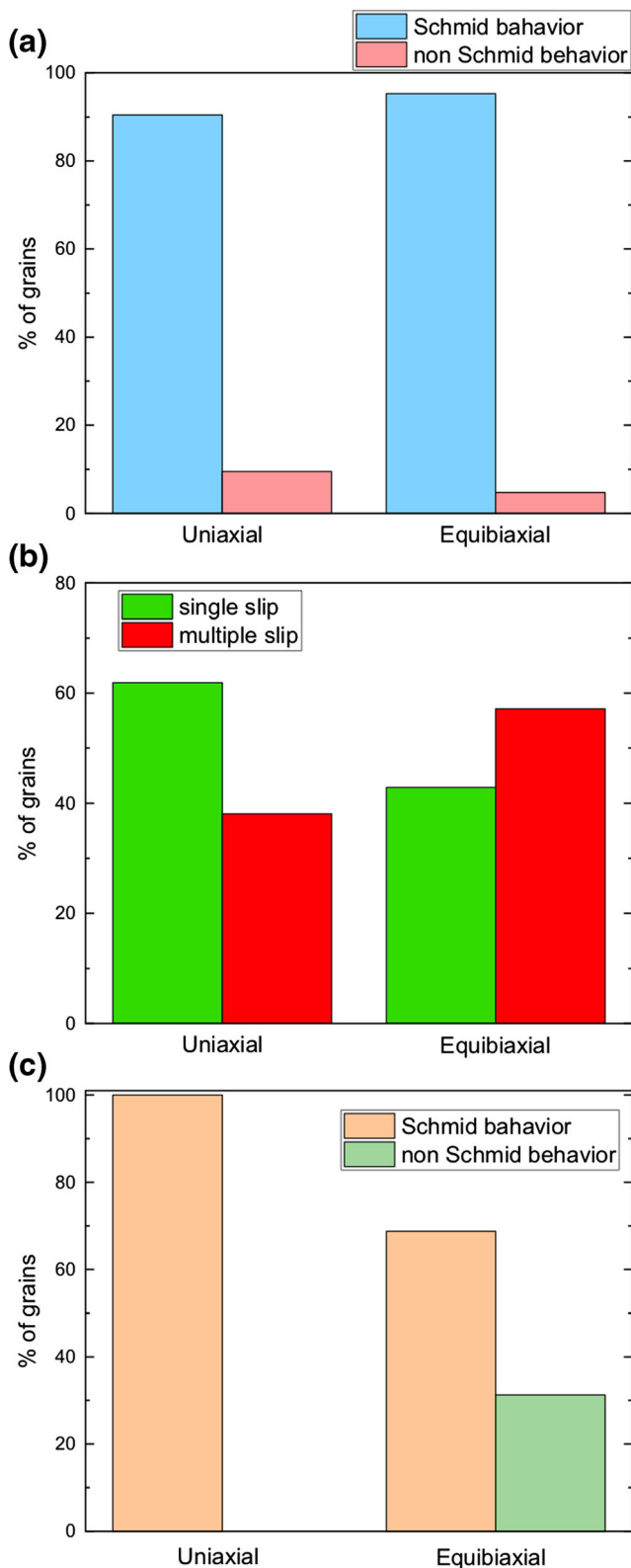
Global 2%   Global 6%   Global 10%   Global 14%

Equivalent Strain

0.35
0.3
0.25
0.2
0.15
0.1
0.05
0

this explanation and shows that in-situ HRDIC provides statistically relevant information at the grain level for the observed difference in the martensite formation under uniaxial and equibiaxial loading at large strains. Further quantitative investigation of the deformation-induced martensite and of the dominant deformation mechanisms under different load paths is the scope of another study.

Conclusions

A miniaturized biaxial cruciform geometry is presented that allows combining HRDIC in-situ during uniaxial and biaxial deformation. Utilizing electrochemical micromachining for preparing the sample geometry offers: i) thickness reduction at the center of the cruciform and concentration of uniform deformation at the center and ii) excellent surface quality allowing EBSD characterization and HRDIC studies after deposition of gold particles. The experimental mechanical results are in good agreement with FE simulations, allowing for estimating the stress values at the center of the cruciform sample for the strain values at which HRDIC was performed. Application of this new geometry combined with HRDIC on SS304 shows that after yielding, the activated {111}<110> slip systems are in good agreement with the Schmid law for the majority of the grains. For similar equivalent strain values, equibiaxial loading activates more slip systems compared to uniaxial loading, which according to the martensite nucleation theory would increase the deformation-induced martensite nucleation sites.

References

1. Grässel O, Krüger L, Frommeyer G, Meyer LW (2000) High strength Fe–Mn–(Al, Si) TRIP/TWIP steels development — properties — application. Int J Plast 16:1391–1409
2. Talonen J, Hänninen H, Nenonen P, Pape G (2005) Effect of strain rate on the strain-induced $\gamma \rightarrow \alpha'$-martensite transformation and mechanical properties of austenitic stainless steels. Metall Mater Trans A 36:421–432
3. Tasan CC, Hoefnagels JPM, Dekkers ECA, Geers MGD (2012) Multi-Axial Deformation Setup for Microscopic Testing of Sheet Metal to Fracture. Exp Mech 52:669–678

Fig. 9 Statistical analysis showing (a) the fraction of grains obeying the Schmid law for the activation of the primary slip system, (b) the fraction of grains in which single or multiple slip system activation occurs and (c) the fraction of grains obeying the Schmid law for the activation of the secondary/tertiary slip systems, under uniaxial and equibiaxial loading

4. Polatidis E, Hsu WN, Šmíd M, Panzner T, Chakrabarty S, Pant P, Van Swygenhoven H (2018) Suppressed martensitic transformation under biaxial loading in low stacking fault energy metastable austenitic steels. Scr Mater 147:27–32

5. Martin S, Ullrich C, Rafaja D (2015) Deformation of Austenitic CrMnNi TRIP/TWIP Steels: Nature and Role of the ε−martensite. Mater Today 2:S643–S646

6. Talonen J, Hänninen H (2007) Formation of shear bands and strain-induced martensite during plastic deformation of metastable austenitic stainless steels. Acta Mater 55:6108–6118

7. Allain S, Chateau JP, Bouaziz O, Migot S, Guelton N (2004) Correlations between the calculated stacking fault energy and the plasticity mechanisms in Fe–Mn–C alloys. Mater Sci Eng A 387-389:158–162

8. Martin S, Wolf S, Martin U, Krüger L, Rafaja D (2016) Deformation Mechanisms in Austenitic TRIP/TWIP Steel as a Function of Temperature. Metall Mater Trans A 47:49–58

9. Byun TS, Hashimoto N, Farrell K (2004) Temperature dependence of strain hardening and plastic instability behaviors in austenitic stainless steels. Acta Mater 52:3889–3899

10. Van Petegem S, Wagner J, Panzner T, Upadhyay MV, Trang TTT, Van Swygenhoven H (2016) In-situ neutron diffraction during biaxial deformation. Acta Mater 105:404–416

11. Hsu W-N, Polatidis E, Šmíd M, Casati N, Van Petegem S, Van Swygenhoven H (2018) Load path change on superelastic NiTi alloys: In situ synchrotron XRD and SEM DIC. Acta Mater 144:874–883

12. Li D-F, O'Dowd NP (2011) On the evolution of lattice deformation in austenitic stainless steels—The role of work hardening at finite strains. J Mech Phys Solids 59:2421–2441

13. Caër C, Pesci R (2017) Local behavior of an AISI 304 stainless steel submitted to in situ biaxial loading in SEM. Mater Sci Eng A 690:44–51

14. Collins DM, Erinosho T, Dunne FPE, Todd RI, Connolley T, Mostafavi M, Kupfer H, Wilkinson AJ (2017) A synchrotron X-ray diffraction study of non-proportional strain-path effects. Acta Mater 124:290–304

15. Kulawinski D, Nagel K, Henkel S, Hübner P, Fischer H, Kuna M, Biermann H (2011) Characterization of stress–strain behavior of a cast TRIP steel under different biaxial planar load ratios. Eng Fract Mech 78:1684–1695

16. Hannon A, Tiernan P (2008) A review of planar biaxial tensile test systems for sheet metal. J Mater Process Technol 198:1–13

17. Van Petegem S, Guitton A, Dupraz M, Bollhalder A, Sofinowski K, Upadhyay MV, Van Swygenhoven H (2017) A Miniaturized Biaxial Deformation Rig for in Situ Mechanical Testing. Exp Mech 57:569–580

18. Upadhyay MV, Panzner T, Van Petegem S, Van Swygenhoven H (2017) Stresses and Strains in Cruciform Samples Deformed in Tension. Exp Mech 57:905–920

19. Das YB, Forsey AN, Simm TH, Perkins KM, Fitzpatrick ME, Gungor S, Moat RJ (2016) In situ observation of strain and phase transformation in plastically deformed 301 austenitic stainless steel. Mater Des 112:107–116

20. Di Gioacchino F, Quinta da Fonseca J (2013) Plastic Strain Mapping with Sub-micron Resolution Using Digital Image Correlation. Exp Mech 53:743–754

21. Di Gioacchino F, Quinta da Fonseca J (2015) An experimental study of the polycrystalline plasticity of austenitic stainless steel. Int J Plast 74:92–109

22. Lunt D, Busolo T, Xu X, Quinta da Fonseca J, Preuss M (2017) Effect of nanoscale α2 precipitation on strain localisation in a two-phase Ti-alloy. Acta Mater 129:72–82

23. Orozco-Caballero A, Lunt D, Robson JD, Quinta da Fonseca J (2017) How magnesium accommodates local deformation

incompatibility: A high-resolution digital image correlation study. Acta Mater 133:367–379

24. Chen Z, Daly SH (2017) Active Slip System Identification in Polycrystalline Metals by Digital Image Correlation (DIC). Exp Mech 57:115–127

25. Kammers AD, Daly S (2013) Digital Image Correlation under Scanning Electron Microscopy: Methodology and Validation. Exp Mech 53:1743–1761

26. Platt P, Lunt D, Polatidis E, Wenman MR, Preuss M (2016) In-situ digital image correlation for fracture analysis of oxides formed on zirconium alloys. Corros Sci 111:344–351

27. Tasan CC, Hoefnagels JPM, Geers MGD (2010) Microstructural banding effects clarified through micrographic digital image correlation. Scr Mater 62:835–838

28. Landolt D, Chauvy PF, Zinger O (2003) Electrochemical micromachining, polishing and surface structuring of metals: fundamental aspects and new developments. Electrochim Acta 48:3185–3201

29. ABAQUS (2011) AD. DassaultSystèmes, Providence

30. micropat SA (2018) http://www.micropat.ch. Accessed 7 August 2018

31. Chauvy P-F, Hoffmann P, Landolt D (1992) Electrochem. Solid-State Lett 4:C31–C34

32. West A C, Madore C, Matlosz M, Landolt D (1992) Shape changes during through-mask electrochemical micromachining of thin metal films. J Electrochem Soc 139:499–506

33. Blaber J, Adair B, Antoniou A (2015) Ncorr: Open-Source 2D Digital Image Correlation Matlab Software. Exp Mech 55:1105–1122

34. Reu P (2015) Virtual strain gage size study. Exp Tech 39:1–3

35. Sutton MA, Li N, Joy DC, Reynolds AP, Li X (2007) Scanning Electron Microscopy for Quantitative Small and Large Deformation Measurements Part I: SEM Imaging at Magnifications from 200 to 10,000. Exp Mech 47:775–787

36. Sutton MA, Li N, Garcia D, Cornille N, Orteu J-J, McNeill SR, Schreier HW, Li X (2007) Scanning Electron Microscopy for Quantitative Small and Large Deformation Measurements Part II: Experimental Validation for Magnifications from 200 to 10,000. Exp Mech 47:789–804

37. Xu Z-H, Li X-D, Sutton MA, Li N (2008) Drift and spatial distortion elimination in atomic force microscopy images by the digital image correlation technique. J Strain Anal Eng Des 43:729–743

38. Li N, Sutton MA, Li X, Schreier HW (2008) Full-field Thermal Deformation Measurements in a Scanning Electron Microscope by 2D Digital Image Correlation. Exp Mech 48:635–646

39. Xu Z-H, Jin H, Lu W-Y, Sutton MA, Li X (2011) Influence of Scanning Rotation on Nanoscale Artificial Strain in Open-Loop Atomic Force Microscopy. Exp Mech 51:619–624

40. Zhu T, Sutton MA, Li N, Orteu J-J, Cornille N, Li X, Reynolds AP (2011) Quantitative Stereovision in a Scanning. Electron Microscope Exp Mech 51:97–109

41. Hecker SS, Stout MG, Staudhammer KP, Smith JL (1982) Effects of Strain State and Strain Rate on Deformation-Induced Transformation in 304 Stainless Steel: Part I. Magnetic Measurements and Mechanical Behavior. Metall Trans A 13:619–626

42. Murr LE, Staudhammer KP, Hecker SS (1982) Effects of Strain State and Strain Rate on Deformation-Induced Transformation in 304 Stainless Steel: Part II. Microstructural Study. Metall Trans A 13:627–635

43. Olson GB, Cohen M (1972) A mechanism for the strain-induced nucleation of martensitic transformations. J Less Common Met 28:107–118

44. Olson GB, Cohen M (1975) Kinetics of strain-induced martensitic nucleation. Metall Trans A 6:791–795